*Technical Report*

# Investigation on Reduction Behavior of Multi Component Calcium Ferrites by *In Situ* XRD/XAFS

Reiko MURAO* Masao KIMURA


## Abstract

***Multi component calcium ferrites included in iron ore sinter as bonding components represent various crystal structures, compositions, and fine textures, and therefore, they affect reducibility of the sinter. To clarify the reduction behavior, in situ observation at 900°C under hydrogen atmosphere of various multi-component calcium ferrites was conducted by using X-ray diffraction (XRD) and X-ray absorption spectroscopy (XAS). Multi component calcium ferrites consist of a layered structure of spinel and pyroxene were found to be decompose into these units at the early stage of the reduction reaction. The spinel was reduced sequentially into FeOx then Fe. The intermediate component $Ca_2(Fe, Al)_2O_5$ originated in the pyroxene module was difficult to reduce and the reaction was controlled by decomposition of this phase.***


## 1. Introduction

Multi-component calcium ferrite refers to complex oxides such as Ca, Fe, Al, and Si contained in sintered ore, a blast furnace raw material. The basic structure of sintered ore consists of iron ore grains, a bonding layer, voids, and cracks.[1] The bonding layer contains multiple phases, including quasi-binary calcium ferrites ($CaO–Fe_2O_3$) precipitated from the melt, multicomponent calcium ferrites (silico-ferrites of calcium and aluminum: SFCA), $CaO–SiO_2$ glass (slag component), and solid solutions of these. The microstructure of the final product, sintered ore, is strongly influenced by various reactions and the accompanying phase formation during the heating and cooling processes of the sintering process.[2, 3] The bonding layer, composed of multicomponent calcium ferrite, adopts multiple crystal structures depending on composition and formation temperature. Since it constitutes approximately 30% of the solid phase in sintered ore,[4] the types, quantities, and microstructure of these phases are considered to significantly contribute to the properties of the sintered ore (strength, reducibility, reduction disintegration, etc.). Representative multicomponent calcium ferrites in sintered ore include the SFCA phase and SFCA-I phase, which contain $SiO_2$ and $Al_2O_3$. SFCA and SFCA-I adopt structures related to the Aenigmatite group of mineral phases and can be represented as $M_{14+6n}O_{20+8n}$ ($n$=0, 1), respectively. The SFCA phase has the structure $A_2M_6T_6O_{20}$, while the SFCA-I phase has $A_3BM_8T_8O_{28}$ (A=$Ca^{2+}$; B = $Ca^{2+}$, $Fe^{2+}$, M (octahedral site)=$Fe^{3+}$; T (tetrahedral site)=$Fe^{3+}$, $Al^{3+}$, $Si^{4+}$). As shown in **Fig. 1**[5], the crystal structures of these phases consist of layered structures corresponding to Spinel (S) and Pyroxene (P). The unit cell repetition for SFCA is -S-P-S-P-, while for SFCA-I it is -S-S-P-S-S-P-. Furthermore, single crystal structure analysis has reported the existence of the SFCA-II phase with a layered structure of -S-S-P-S-P- and the SFCA-III phase with -S-S-S-P- ($M_{14+6n}O_{20+8n}$, $n$=2).[6, 7] The SFCA-II phase, which does not contain Si, is reported to form in the continuous solid solution range of $CaAl_3O_{10}–CaFe_3O_{10}$, with $Fe_2O_3$ occurring in the composition range of 44.5–81.5 mol%.[8, 9] However, its formation mechanism is not yet fully understood. No examples of SFCA-II being present in sintered ore have been reported.

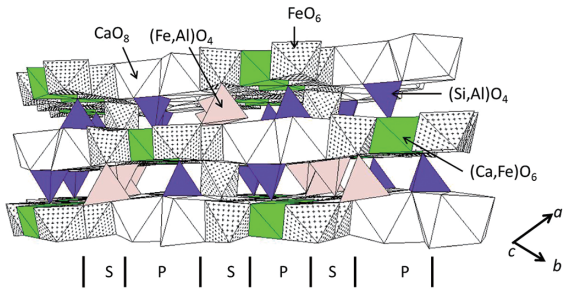


**Fig. 1 Crystal structure of SFCA, indicating layered structure of spinel (S) and pyroxene (P) modules**

* Dr. Eng., Chief Manager, Head of Dept., Materials Characterization Research Lab., Advanced Technology Research Laboratories
20-1 Shintomi, Futtsu City, Chiba Pref. 293-8511

These phases form a continuous solid solution, where the charge balance is maintained by the substitution mechanism $2(Fe^{3+}, Al^{3+}) = (Ca^{2+}, Fe^{2+}) + Si^{4+}$. They are known to possess a broad solid solution range,[10] but the formation regions and physical properties remain incompletely understood. Furthermore, single crystal structure analysis has been performed on the SFCAM phase containing Mg solid solution[10].

The crystal structure of multicomponent calcium ferrite was elucidated relatively recently (since 1989). While the equilibrium state of calcium ferrite in the $Fe_2O_3$–FeO–CaO system with respect to oxygen partial pressure has been well studied, multicomponent calcium ferrites containing Al and Si were thought to exhibit different high-temperature properties due to significant differences in crystal structure characteristics compared to pseudo-binary systems. However, the details remained poorly understood. This lack of understanding stemmed not only from the complexity of the crystal structure but also from the difficulty of directly observing the formation reactions, such as through *in situ* observation, resulting in limited information on the non-equilibrium reactions occurring during the actual sintering process. Sugiyama et al. reported that reducing the SFCA-I phase and SFCA phase at an oxygen partial pressure of $1 \times 10^{-9.1}$ Pa for 48 hours yielded products of $FeO + Fe_3O_4 + Ca_2Fe_2O_5$ and $Ca_2SiO_4 + FeO + Fe_3O_4 + Ca_2Fe_2O_5$, respectively.[11] Furthermore, Maeda et al. investigated the relationship between the final reduction reaction temperature and the $CO/CO_2$ partial pressure ratio for a quaternary calcium ferrite system ($71.4Fe_2O_3$–$15.1CaO$–$5.7SiO_2$–$7.8Al_2O_3$ (mass%)).[12] Maruoka et al. investigated the reducibility of SFCA and SFCA-I with various compositions under CO–$CO_2$–$H_2$–$H_2O$ atmospheres from 200°C to 800°C. They reported that the reduction of SFCA and SFCA-I did not occur up to 800°C in a CO–$CO_2$ atmosphere up to 800°C, whereas it was promoted in a CO–$CO_2$–$H_2$–$H_2O$ atmosphere. Furthermore, SFCA-I reduces even at 500°C in a CO–$CO_2$ atmosphere. While the Fe concentration in SFCA does not affect its reducibility, the reducibility of SFCA-I is promoted by increasing its Fe concentration.[13]

Therefore, our research group has developed *in situ* observation techniques at high temperatures using various structural analysis methods involving X-rays and synchrotron radiation. We are applying these techniques to elucidate the elementary reactions within the non-equilibrium, heterogeneous ironmaking process. As part of our sintering reaction analysis, we have previously investigated the formation process of calcium ferrite and the reduction reaction. In analyzing the calcium ferrite formation process, we observed the precipitation of calcium ferrite from the $Fe_2O_3$–CaO melt using high-temperature X-ray diffraction (XRD) and high-temperature laser microscopy, and constructed a continuous cooling transformation (CCT) curve.[14] We sought to extend this technique to multicomponent systems. However, since no thermodynamic model for multicomponent calcium ferrite existed for the thermodynamic calculations of the reference equilibrium state, we developed a model considering its crystallographic characteristics.[5]

The reducibility of sintered ore is generally evaluated using the RI test (JIS M8713:2017). This evaluation method assesses bulk samples by isothermal reduction in an $N_2$–30 vol% CO atmosphere at 900°C for 180 minutes. It includes not only the reduction rate intrinsic to each phase (due to phase-specific chemical reactions, independent of topology or surrounding microstructure effects) but also contributions from the microstructure formed by pores within the sintered ore and the shape and distribution of each phase. Multicomponent calcium ferrite in sintered ore precipitates from the melt, adopting various morphologies such as columnar, acicular, or fine-grained depending on the formation process. It further exhibits complex microstructures, sometimes surrounded by silicate slag or occurring in voids. The composition and basicity of the melt are altered by adjacent gangue, influencing the calcium ferrite formation process.[15–18] The reducibility of calcium ferrite is thought to be influenced by both its composition and microstructure. Sakamoto et al. attempted to quantify the reducibility of sintered ore textures and demonstrated that a one-interface unreacted core model, considering gas-phase diffusion reactions within the boundary layer and product layer diffusion processes, agreed relatively well with experimental data.[19] Furthermore, they synthesized single-mineral structures of characteristic phases found in sintered ore to evaluate reducibility, revealing that fine-grained hematite and fine-grained calcium ferrite exhibit high reducibility, while that of ribbon-shaped calcium ferrite crystallized in slag melt is significantly lower. Cai et al. compared the reducibility of columnar calcium ferrite and needle-shaped calcium ferrite, reporting that needle-shaped calcium ferrite, surrounded by fine pores, exhibits better reducibility than columnar calcium ferrite covered by slag.[20] Furthermore, Murakami et al. investigated the effect of coexisting microstructures on reducibility and reported that reducibility deteriorates in the following order: 1H (primary hematite)-ACF (acicular calcium ferrite), 2H (secondary hematite)-CF, Magnetite-ACF, and Magnetite-CCF (columnar calcium ferrite).[21] Details regarding the crystal structure, crystal morphology, and formation process of SFCA have been thoroughly reviewed by Nicol et al.[22] However, it is also necessary to elucidate the intrinsic reduction behavior of each phase contained within sintered ore. Our research group first analyzed the reduction reactions of $Fe_2O_3$ and the pseudo-binary system $CaFe_2O_4$ using X-ray absorption spectroscopy (XAS).[23] In this study,[24] to clarify the influence of crystal structure and composition on the reduction behavior of multicomponent calcium ferrites, we performed *in situ* observation of the high-temperature reduction behavior of various multicomponent calcium ferrite phases with different $Al_2O_3$ solid solution contents at 900°C and analyzed the reduction process. A particularly distinctive aspect of our approach was the use of complementary techniques to achieve a comprehensive understanding of the reaction. Intermediate products were identified by high-temperature XRD measurements. Changes in the valence and coordination numbers of Fe and Ca during the high-temperature reduction reaction were observed using *in situ* XAFS (X-ray absorption fine structure), a representative technique of XAS methods. This allowed the reaction rate to be determined from both the crystal structure and the chemical state of the elements. Furthermore, in addition to high-temperature XRD and XAFS, the results of thermal analysis capable of distinguishing the initiation and completion of the reaction were integrated to examine the reaction process.

## 2. Experiments

### 2.1 Sample

A single-phase calcium ferrite was synthesized using the powder sintering method. $\alpha$-$Fe_2O_3$, $CaCO_3$, $SiO_2$ (quartz), and $\alpha$-$Al_2O_3$ were mixed in a chemically stoichiometric ratio as shown in **Table 1** using an agate mortar, then pressed and formed. After pre-sintering at 800°C for over 2 hours, the samples were re-ground, pressed, and sintered at 1 180°C to 1 230°C for 48 hours. Powder obtained by grinding the resulting calcium ferrite in an agate mortar was used as the sample for reduction experiments. SFCA-I contained a small amount of $Fe_2O_3$, but the other samples were essentially single-

**Table 1 Nominal composition of samples**

(mol%)

| Sample | $Fe_2O_3$ | CaO | $Al_2O_3$ | $SiO_2$ |
|---|---|---|---|---|
| $CaFe_2O_4$ | 50.0 | 50.0 | - | - |
| $Ca_2Fe_2O_5$ | 33.3 | 66.6 | - | - |
| $Ca_2(Al_{0.5},Fe_{0.5})_2O_5$ | 16.67 | 66.67 | 16.67 | - |
| SFCA-I | 67.69 | 25.59 | 6.72 | - |
| SFCA (5) | 56.09 | 30.35 | 5.74 | 7.82 |
| SFCA (15) | 50.37 | 27.34 | 17.11 | 5.17 |

*SFCA-I: $Ca_3(Ca,Fe)(Fe,Al)_{16}O_{28}$, SFCA: $Ca_2(Fe,Ca)_6(Fe,Al,Si)_6O_{20}$

phase at the powder XRD level, with impurity crystalline phases estimated to be less than 1%.

### 2.2 Thermal analysis

Approximately 20 mg of sample powder was lightly filled into an $Al_2O_3$ container without compaction and subjected to thermogravimetry-differential thermal analysis (TG-DTA). A corrosion-resistant sample holder with the R thermocouple junction inside an $Al_2O_3$ protection tube was used. The atmospheric gas pressure and flow rate were set to 0.1 MPa and 150 ml/min, respectively. The sample was heated in an Ar–20 vol% $O_2$ atmosphere. After reaching 900°C, the atmosphere was switched to Ar–3 vol% $H_2$, and the sample was isothermally held for 60–150 min while measuring the weight change.

### 2.3 High-temperature *in situ* X-ray diffraction measurement

The sample powder was filled into a black quartz glass holder with a depth of 0.3 mm and heated upto 900°C in a corrosion-resistant infrared heating furnace installed in the X-ray diffractometer. Heating was performed in air. At 900°C, while maintaining isothermal conditions, a mixture of $N_2$–2 vol% $H_2$ gas was introduced for reduction. The atmospheric gas pressure and flow rate were set to 0.1 MPa and 150 ml/min, respectively, to ensure sufficiently rapid diffusion of the reducing gas within the sample. A Cu tube (tube voltage 40 kV, tube current 40 mA) was used as the X-ray source, and a high-speed one-dimensional semiconductor detector was used as the detector. XRD measurements were repeatedly performed over the $2\theta = 10°–45°$ range with a scan speed of 40°/min. The sample temperature was measured using a K-type sheathed thermocouple inserted into the sample holder.

### 2.4 *In situ* XAFS measurements

*In situ* XAFS experiments were conducted at the Photon Factory (PF), BL-9A, at the High Energy Accelerator Research Organization (KEK) Synchrotron Radiation Research Facility. The quick-XAFS method, involving continuous scanning of a Si(111) double-crystal monochromator, was employed for short-time measurements to obtain XAFS spectra at the Fe or Ca *K*-edge under high-temperature reducing atmospheres. Details of the gas-flow-type cell used for *in situ* observation have been reported previously; therefore, only the measurement conditions are described here.[23, 25] For the Fe *K*-edge XAFS measurements, the starting material calcium ferrite was mixed and diluted with 80 mg of BN powder to achieve an edge jump $\Delta\mu t$ ($=-\ln I/I_0$) of approximately 1 in the XAFS spectrum. The mixture was then hand-pressed and molded into a cylindrical sample holder made of SUS with an inner diameter of 7 mm, which served as the measurement sample. Here, $\mu$ is the linear absorption coefficient of the sample, $t$ is the sample thickness, $I$ is the X-ray intensity transmitted through the sample, and $I_0$ is the incident X-ray intensity. For the Ca *K*-edge XAFS measurement, due to significant X-ray absorption by BN, BN amount was set to 20 mg and adjusted so that the difference in $\mu t$ between the start and end points of the measurement was 4 or less. The samples were heated in an oxidizing atmosphere to 900°C. After reaching 900°C, the atmospheric was switched to He–20 vol% $H_2$, and XAFS spectra were repeatedly measured. The atmosphere gas pressure and flow rate were set to 0.1 MPa and 200 ml/min, respectively, ensuring sufficiently rapid diffusion of reducing gas within the sample. For the Fe *K*-edge and Ca *K*-edge measurement cycles, the energy range $6911 < E < 7581$ eV was swept in 21 seconds, and the range $3990 < E < 4140$ eV was swept in 51 seconds.

XAFS spectrum analysis was performed using the EXAFS data analysis software ATHENA (Demeter 0.9.25).[26] Background correction was applied by fitting the data to the Victreen approximation ($C\lambda^3 - D\lambda^4 + \text{const.}$). The EXAFS oscillation was extracted by interpolation using a spline function (Cook-Sayers). For the resulting $k^3\chi(k)$, the radial distribution function was obtained by Fourier transformation in the range $20 < k < 120$ nm$^{-1}$ for Fe and $20 < k < 100$ nm$^{-1}$ for Ca.

## 3. Experimental Results

### 3.1 Thermal analysis

**Figure 2**[24] shows the reduction rate curve and the first derivative of the thermogravimetric (TG) curve obtained from the TG curve of the sample with the composition shown in Table 1 after the start of reduction at 900°C. Here, the reduction rate is the ratio of the oxygen removed to the oxygen bound to iron before reduction, and all iron before the start of reduction was considered to be in the $Fe^{3+}$ state. The reaction start time can be determined from the shape of the first derivative of the TG curve. $Fe_2O_3$ began weight loss 18 minutes after atmospheric gas switching, reducing via $Fe_3O_4$ and FeO to metallic Fe after 60 minutes. The reaction onset times for $CaFe_2O_4$ and SFCA-I were nearly identical to that of $Fe_2O_3$. The reduction starting time of SFCA(5) was 18 min, which was earlier than those of SFCA-I and SFCA(15) (20 min for latter). The pres-

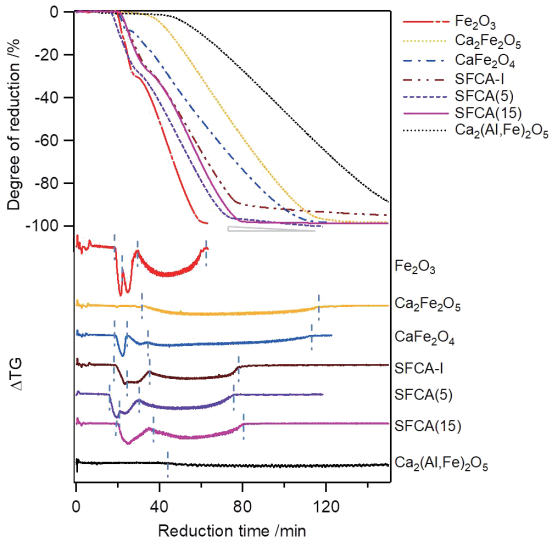


**Fig. 2 Reduction time dependence of degree of reduction and differential of thermogravimetric curves of samples in Ar–3 vol% $H_2$ atmosphere at 900°C**

ence of multiple inflection points on the derivative curves indicates that the reaction processes for $CaFe_2O_4$, SFCA-I, and SFCA involve at least three distinct stages. $Ca_2(Al_{0.5},Fe_{0.5})_2O_5$ was difficult to reduce, with a reduction start time of 45 minutes. The reaction ends of $CaFe_2O_4$ and $Ca_2Fe_2O_5$ were 120 min, whereas the reaction of SFCA was considerably gradual, occurring at approximately 75 min.

### 3.2 *In situ* XRD

**Figure 3**(a) shows the time evolution of the XRD pattern of $CaFe_2O_4$ at 900°C under a reducing atmosphere. Intermediate phases were identified as $CaFe_3O_5$, $CaFe_5O_7$, and $Ca_2Fe_2O_5$. As reduction progressed, the phases changed as follows: $Ca_2Fe_2O_5+FeO \rightarrow Ca_2Fe_2O_5+CaO+FeO+Fe \rightarrow CaO+Fe$. The coexistence of $Ca_2Fe_2O_5$, FeO, and Fe indicates that the reduction of the hard-to-reduce $Ca_2Fe_2O_5$ is the rate-limiting step. These reaction processes are in good agreement with the CO–$CO_2$ equilibrium Baur-Glaessner diagram[27] and the thermogravimetric analysis results.

Similarly, Fig. 3(b) and (c) show the time-dependent XRD patterns of SFCA-I and SFCA(5) at 900°C under a reducing atmosphere. Figure 3(d)[24] shows the XRD patterns of $CaFe_2O_4$, SFCA-I, SFCA(5), and SFCA(15) 3 minutes after the start of reduction. During the reduction of the SFCA-I phase, $Fe_3O_4$ and $Ca_2(Fe,Al)_2O_5$ were identified as intermediate products. $Fe_3O_4$ was reduced to metallic iron via FeO. The diffraction intensity of $Ca_2(Fe,Al)_2O_5$ remained almost unchanged even after 90 minutes, and unlike in the case of $CaFe_2O_4$, no CaO formation was observed. Three minutes after reduction initiation, the diffraction lines for SFCA(5) had almost disappeared, and diffraction lines for $Fe_3O_4$, FeO, and $Ca_2(Fe,Al)_2O_5$ were observed. After 90 minutes, it became a mixture of Fe, FeO, $Ca_2(Fe,Al)_2O_5$, and $Ca_2SiO_4$. The diffraction intensity of $Ca_2(Fe,Al)_2O_5$ showed a decreasing trend. Furthermore, the high scattering intensity near $2\theta=35°$ suggests the possible formation of an amorphous Ca–Si–O. Although SFCA(15) exhibited a slower reduction rate compared to SFCA(5), the intermediate phase was identical. Therefore, the reduction reaction process is considered to be the same as for SFCA(5), differing only in reduction rate. It is inferred that the crystalline structure of SFCA tends to be more difficult to reduce as the Al content increases.

### 3.3 *In situ* XAFS

#### 3.3.1 Local structural changes around Fe

**Figure 4**(a) shows the Fe *K*-edge XAFS spectra of $CaFe_2O_4$, SFCA-I, and SFCA(5) measured at room temperature before reduction and after reduction treatment at 900°C for 80 minutes. For comparison, the spectra of metallic iron, FeO, $Fe_3O_4$, and $\alpha$-$Fe_2O_3$ are also shown. The absorption edge position shifts toward higher energies with increasing Fe valence, and oxides tend to exhibit higher intensity in the white line (the absorption peak immediately above the absorption edge). The pre-edge energy value is $Fe^{2+}<Fe^{3+}$, and the pre-edge intensity shows a 4-coordination>6-coordination trend. The Fe contained in both unreduced $CaFe_2O_4$ and SFCA is $Fe^{3+}$. SFCA contains a small amount of $Fe^{2+}$, but at a level undetectable by XAFS. Since Fe in SFCA occupies both 4-coordinate and 6-coordinate oxygen sites, the pre-edge peak intensity tends to be higher than in $CaFe_2O_4$ or $Fe_2O_3$, which contain only 6-coordinate sites. The spectral shape after reduction closely matches that of Fe. Figure 4(b) shows the radial distribution function (RDF) around Fe obtained by Fourier transforming the XAFS spectrum. In the reduced sample, the first-neighbor Fe–O correlation peak observed before reduction has almost disappeared, and a Fe–Fe correlation peak characteristic of metallic iron is observed.

**Figure 5**(a)–(c)[24] shows the time evolution of the Fe *K*-edge XAFS spectra for $CaFe_2O_4$, SFCA-I, and SFCA(5) under a reducing atmosphere at 900°C. $CaFe_2O_4$ exhibited a spectrum close to metal-

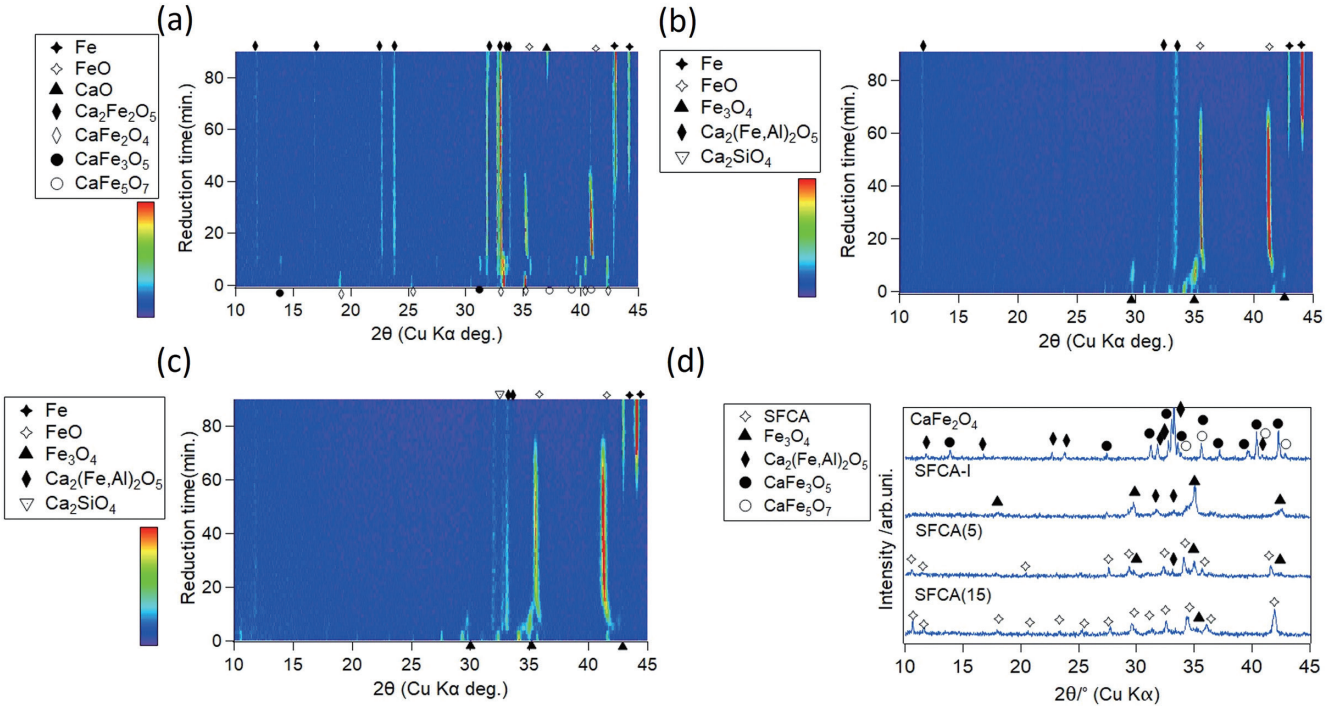


**Fig. 3** ***In situ*** **XRD patterns at 900°C**
**Reduction time dependence of (a) $CaFe_2O_4$, (b) SFCA-I, and (c) SFCA(5). (d) Profiles reduced for three minutes.**

lic Fe after 20 min of reduction, whereas SFCA-I and SFCA(5) showed spectra characteristic of mixtures of iron oxide and metallic iron.

**Figure 6**(a)[24] shows the time evolution of the normalized absorbance at the energy position indicated by the arrow in Fig. 5(c) for SFCA(5). The time axis starts at 0 minutes when $H_2$ gas introduction began. At least three distinct intensity changes were observed between the start of reducing gas introduction and 19 minutes, indicating reduction to FeO via multiple intermediate products containing both $Fe^{2+}$ and $Fe^{3+}$. The spectral shape between 5–10 minutes after reduction initiation resembles that of $Fe_3O_4$, consistent with the observation of $Fe_3O_4$ diffraction in XRD. After 19 minutes, equal absorption points (points where the absorption rate is the same at all times) exist at 7120 eV and 7143 eV. The XAFS spectrum of the mixture is a superposition of the spectra of its constituent phases, and the absorbance is the sum of the products of the molar concentration and absorbance of each phase. The presence of isosbestic points indicates that only two components (phases) exist in the reaction system, meaning one phase gradually transforms into another. Therefore, the reaction after 19 minutes from the start of reduction was considered a pseudo-first-order reaction $[Fe^{2+} \rightleftarrows (1-f)Fe^{2+} + fFe^0]$, approximated by the first-order rate equation $[A]=[A]_0 e^{-k1x}$, and the reaction rate was derived. Here, $[A]$ is the molar concentration of the reactant, $[A]_0$ is the initial molar concentration of the reactant, and $x$ is the reaction time, corresponding to the FeO concentration in the SFCA(5) reduction process. Specifically, using the normalized absorbance $\mu t$ at 7125 eV after 19 minutes of reduction initiation, as shown in Fig. 6(a), was fitted by the least-squares method using the function $\mu t = y_0 + ae^{k1(x-x_0)}$. Here, $\mu t$ is the absorbance, $y_0$ and $a$ are constants, $x$ is the reaction time, and $x_0$ is the reaction start time; for SFCA(5), $x_0$=19 min. As a result, the reaction rate constant $k_1$ was determined to be $k_1$=0.31(2) $min^{-1}$. In the reduction reaction of $CaFe_2O_4$, an equimolar point is observed after 13 minutes from the start of reduction. In this region, the reduction reactions $Ca_2Fe_2O_5 \rightarrow 2CaO + 2FeO$ and $FeO \rightarrow Fe$ occur sequentially. However, $Ca_2Fe_2O_5 \rightarrow 2CaO + 2FeO$ is the rate-limiting step, and FeO is rapidly reduced to Fe even after its formation. Therefore, for the absorbance at 7125 eV after 13 minutes, a pseudo-first-order reaction $Ca_2Fe_2O_5 \rightarrow 2CaO + 2Fe$ was considered to occur, and it was similarly analyzed using a first-order reaction equation. As a result, the reaction rate constant $k_1$ was determined to be $k_1$=0.147(2) $min^{-1}$.

Figure 6(b)[24] shows the time-dependent changes in normalized absorbance of the white line for $CaFe_2O_4$, SFCA-I, and SFCA(5). The change in absorbance for SFCA-I is more gradual compared to $CaFe_2O_4$ and SFCA(5). The time evolution in absorbance after 33 min from the onset of reduction, at which isosbestic points were observed at 7125 and 7145 eV, were fitted using a first-order reaction equation. As a result, the reaction rate constant, $k_1$, was determined to be $k_1$ = 0.037(2) $min^{-1}$. Based on the changes in the phases observed in the XRD patterns shown in Fig. 3, this behavior is considered to correspond to the reduction reaction from FeO to Fe. Factors contributing to the different behavior compared to SFCA(5) include the higher amount of $Ca_2(Fe,Al)_2O_5$ formed in SFCA-I. The higher solid solution content of Ca and Al in the FeO formed during the

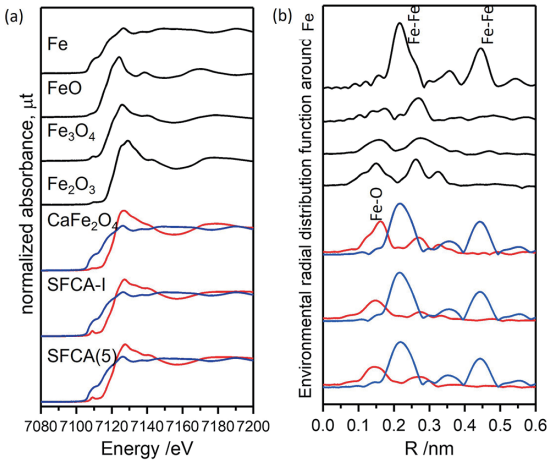


**Fig. 4 (a) Fe *K*-edge XAFS spectra and (b) Environmental RDF around Fe of samples before reduction (red line), and after 80-min reduction at 900°C (blue line)**

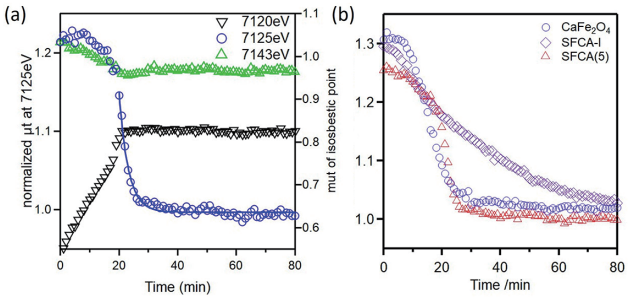


**Fig. 6 (a) Reduction time dependence of normalized absorbance at 7120 eV, 7125 eV, and 7143 eV of SFCA(5)**
**(b) Reduction time dependence of normalized absorbance of the white line of $CaFe_2O_4$, SFCA-I, and SFCA(5)**

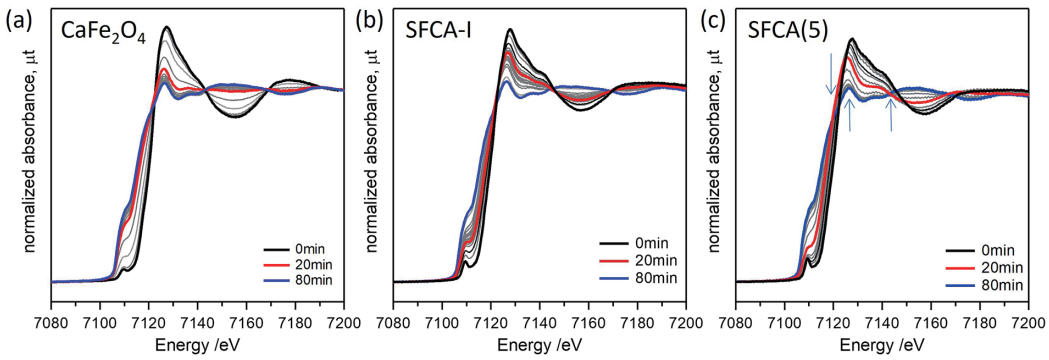


**Fig. 5 *In situ* Fe *K*-edge XAFS spectra in He–20 vol% $H_2$ atmosphere at 900°C**

spinel reduction process is presumed to be the reason for the slower reduction rate compared to SFCA(5).

### 3.3.2 Local structural changes around Ca

**Figure 7**(a)[24] shows the Ca *K*-edge XAFS spectra of $CaFe_2O_4$, SFCA-I, and SFCA(5) before reduction and after reduction treatment at 900°C for 60 minutes. Figure 7(b)[24] shows the RDF around Ca obtained by Fourier transforming the XAFS spectrum in the range $20<k<100$ nm$^{-1}$. For comparison, data for CaO, $CaSiO_3$, and $Ca_2Fe_2O_5$ are also shown. In the hydrogen reduction reaction of calcium ferrite, the Ca valence remains divalent, with only the oxygen coordination structure changing. Ca in $CaFe_2O_4$ has an 8-coordinate oxygen structure. The spectrum after reduction showed a shape close to that of 6-coordinate CaO. In the environmental RDF, correlations up to 0.6 nm, including the first-neighbor Ca–O correlation peak and the second-neighbor Ca–Ca correlation, also closely match CaO, indicating that CaO is formed by reduction.

In contrast, in the SFCA-I crystal structure, Ca occupies one 6-coordinate site, two distorted 7-coordinate sites, and partially substitutes Fe's 6-coordinate sites. In the SFCA crystal structure, Ca occupies two distorted oxygen 8-coordinate sites and further partially substitutes Fe's 6-coordinate sites. The reduced samples of SFCA-I and SFCA(5) exhibit spectra close to $CaSiO_3$ or the unreduced $Ca_2Fe_2O_5$. The correlation peaks observed in the environmental RDF are similar to $Ca_2Fe_2O_5$ but do not match perfectly, suggesting a mixture.

**Figure 8**(a)–(c)[24] shows the time evolution of the Ca *K*-edge XAFS spectrum at 900°C for $CaFe_2O_4$, SFCA-I, and SFCA(5). For $CaFe_2O_4$, the shoulder at 4040 eV nearly disappeared within 10 minutes after reduction initiation, resulting in a CaO spectrum. Equivalent absorption points at 4049 and 4053 eV were observed from the early reduction stage (indicated by arrows in Fig. 8), suggesting that the local structure around Ca changes during the primary reaction. SFCA-I and SFCA(5) exhibited absorption peaks at 4045 eV and 4050.5 eV, respectively, but these peaks disappeared around 10 minutes after reduction initiation, while the absorption peak at 4045.7 eV increased. Both samples showed isosbestic points at 4048.5 eV and 4055 eV from the initial stage of reduction, but the spectral noise was significant, making interpretation difficult.

**Figure 9**[24] shows the time evolution of the normalized absorbance of $CaFe_2O_4$ at $E=4047$ eV and that of SFCA and SFCA-I at 4045.7 eV. Ca in $CaFe_2O_4$ and its reduction reaction intermediates $CaFe_3O_5$, $CaFe_5O_7$, and $Ca_2Fe_2O_5$ has an 8-coordinate oxygen structure, while the final product CaO has a 6-coordinate oxygen structure. Considering this as a primary reaction where the local structure around Ca changes from 8-coordinate to 6-coordinate, the reaction rate constant was determined by fitting the normalized absorbance at $E=4047$ eV. For SFCA-I and SFCA(5), the process where the coordination structure around Ca changes due to the decomposition of the stacked structure of the Pyroxene module and Spinel module

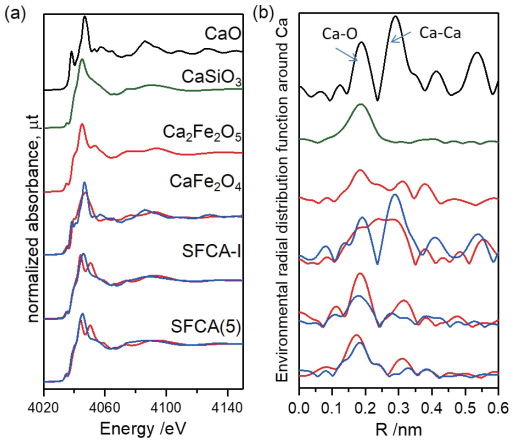


**Fig. 7 (a) Ca *K*-edge XAFS spectra and (b) Environmental RDF around Fe of samples before reduction (red line), and after 60-min reduction at 900°C (blue line)**

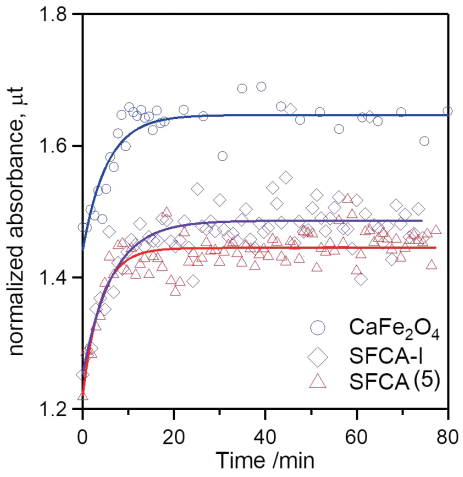


**Fig. 9 Reduction time dependence of normalized absorbance of $CaFe_2O_4$ at 4047 eV, SFCA-I, and SFCA(5) at 4045.7 eV, respectively**

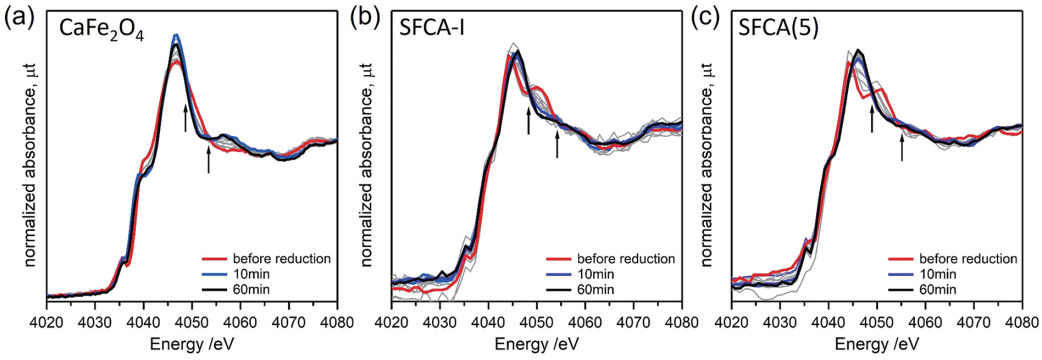


**Fig. 8 *In situ* Ca *K*-edge XAFS spectra in He–20 vol% $H_2$ atmosphere at 900°C**

during the initial reaction phase was considered a first-order reaction. For SFCA(5), multiple phases containing Ca, namely $Ca_2(Fe,Al)_2O_5$ and $Ca_2SiO_4$, were formed. Since $Ca_2(Fe,Al)_2O_5$ further reduced to form $(Fe,Al,Ca)O_x$, it would be preferable to analyze the early and late reaction stages separately. However, detailed analysis was difficult due to the quality of the spectra obtained. Therefore, fitting was performed assuming a pseudo-first-order reaction. As a result, the reaction rate constants for the local structural changes around Ca in $CaFe_2O_4$, SFCA-I, and SFCA(5) were determined to be $k_1 = 0.19(3)/0.16(3)/0.26(3)\ min^{-1}$, respectively.

## 4. Analysis

The crystal structure of the SFCA phase is a modular structure in which spinel ($Fe_3O_4$) and pyroxene ($Ca(Fe,Ca)(Fe,Al,Si)_2O_6$) structures are alternately arranged. The oxides containing Ca, Al, and Si formed during reduction originate from the pyroxene structure. Based on equilibrium experiments conducted under low oxygen partial pressure, the multistep reaction observed in the initial reaction stage is considered to result from the decomposition of these modular structures and the progression of reduction in the spinel structure.[11] High-temperature XRD diffraction peaks for the spinel structure ($Fe_3O_4$) observed during the initial reduction of SFCA-I and SFCA phases indicate that the decomposition of the modular structure occurs at the very beginning of the reduction reaction. Although Ca and Al solid-solve in the spinel structure, resulting in a slower reduction rate than pure $Fe_3O_4$, reduction proceeds more rapidly compared to Fe contained in pyroxene. When the pyroxene structure contains Si, it decomposes into Ca–Si–O and $Ca_2(Fe,Al)_2O_5$. As SFCA(5) reduced, the $Ca_2SiO_4$ diffraction peak grew, while the $Ca_2(Fe,Al)_2O_5$ peak intensity decreased. In contrast, the $Ca_2(Fe,Al)_2O_5$ formed by reducing SFCA-I (high Fe, low Ca) showed no decrease in diffraction peak intensity even after 90 minutes of reduction, as measured by XRD. This crystal structure may exist more stably than $Ca_2(Fe,Al)_2O_5$ in SFCA, depending on the composition ratio of Ca, Al, and $Fe^{2+}$, since $(Ca,Fe^{2+})_2(Fe,Al)_2O_5$ containing $Fe^{2+}$ also exists under low oxygen partial pressure conditions.

These results indicate that the reduction reactions of the SFCA-I and SFCA phases begin with the decomposition of the spinel-pyroxene layered structure within the crystal structure of each phase, as shown in the schematic diagram in **Fig. 10**, followed by the rapid reduction of Fe in the spinel to metallic iron. On the other hand, $Ca_2(Fe,Al)_2O_5$ derived from the pyroxene structure is difficult to reduce, and it is considered that the reduction rate slows down as the concentration of solid solution elements other than Fe, such as Al, increases.

As described above, intermediate products formed during the reduction of calcium ferrite can be identified by *in situ* high-temperature XRD observation. Characterization and kinetic discussions in cases of poor crystallinity can be effectively addressed through XAFS spectrum analysis. Combining *in situ* XAFS, XRD, and thermal analysis enables detailed qualitative and quantitative analysis of reduction element processes within the blast furnace. Although not performed here due to the use of powder samples, future work should include microstructural analysis for phase composition and investigating the distribution of Al and Ca between phases.

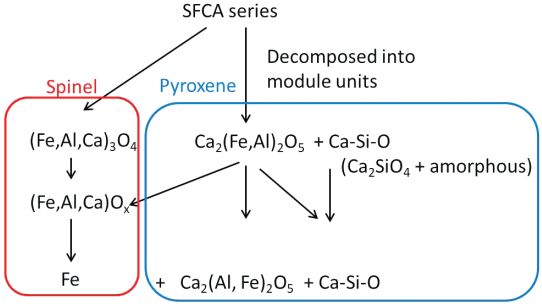


**Fig. 10 Schematic illustration of reduction route of SFCA**

## 5. Conclusion

This study employed a comprehensive approach to observe the reduction behavior of multicomponent calcium ferrite *in situ*: evaluating oxygen desorption processes via weight loss analysis using thermal analysis, identifying intermediate phases using X-ray diffraction, and observing local structural changes in Fe or Ca using X-ray absorption spectroscopy. Each result was quantitatively analyzed, and the obtained insights were combined to examine the reaction process. The reaction temperature was set to 900°C, which is used for evaluating the reduction index (JIS-RI) of sintered ore. The reduction reaction of the SFCA-I and SFCA phases begins with the decomposition reaction of the spinel-pyroxene layered structure within each phase's crystal structure, followed by the rapid reduction of Fe in the spinel to metallic iron. Furthermore, it was clarified that in the case of the Si-free SFCA-I phase, $Ca_2(Fe,Al)_2O_5$ is formed and undergoes slow reduction, while in the Si-containing SFCA phase, it separates into the refractory $Ca_2(Fe,Al)_2O_5$ and Ca–Si–O.

For complex oxides with intricate crystal structures like the SFCA phase, considering structural characteristics in reduction behavior analysis facilitates understanding of the underlying reactions.

Although this study analyzed reduction at 900°C using hydrogen, actual blast furnace reactions occur in a $CO–CO_2–H_2–H_2O$ gas system, with temperature and oxygen partial pressure changing from the initial to final stages. It has been reported that SFCA-I begins reduction at a lower temperature than SFCA at intermediate oxygen partial pressures.[13] To predict the reaction inside the blast furnace, it is necessary to investigate the reduction element reaction temperatures and atmosphere dependence of each phase contained in sintered ore in detail, which is considered a future task.

**Acknowledgments**

X-ray absorption spectroscopy measurements were conducted as part of a joint research project between Nippon Steel Corporation and the High Energy Accelerator Research Organization (Project Numbers: 2012C202, 2013C209, 2015C206). We gratefully acknowledge the analytical support provided by Associate Professor Kenichi Kimishima and Dr. Yohei Kamimura (currently at the Paul Scherrer Institute) from the High Energy Accelerator Research Organization, as well as Mr. Kengo Noami and Mr. Yu Nemoto from Nippon Steel Technology Co., Ltd.

**References**

1) Inazumi, T.: Iron ore sinter -Review of Steps Taken to Overcome the Challenges Posed Japan's Lack of Iron Ore Resources-. Tokyo, ISIJ, 2000, 213p
2) Yazawa, A. et al.: Can. Metall. Q. 20 (2), 129 (1981)
3) Matsuno, F. et al.: Trans. Iron Steel Inst. Jpn. 21, 318 (1981)
4) Takayama, T. et al.: Tetsu-to-Hagané. 103 (6), 397 (2017)
5) Murao, R. et al.: ISIJ Int. 58 (2), 259 (2018)
6) Mumme, W. G.: N. Jb. Miner. Abh. 178 (3), 307 (2003)
7) Kahlenberg, V. et al.: Acta Cryst. B75, 1126 (2019)

8) Dayal, R. R. et al.: Sci. Ceram. 3, 191 (1967)
9) Lister, D. H. et al.: Br. Ceram. Trans. 66 (7), 293 (1967)
10) Sugiyama, K. et al.: ISIJ Int. 45 (4), 560 (2005)
11) Sugiyama, K. et al.: CAMP-ISIJ. 20 (1), 17 (2007)
12) Maeda, T. et al.: Tetsu-to-Hagané. 75 (3), 416 (1989)
13) Maruoka, D. et al.: Tetsu-to-Hagané. 111 (12), 728 (2025)
14) Kimura, M. et al.: ISIJ Int. 53 (12), 2047 (2013)
15) Webster, N. A. S. et al.: ISIJ Int. 53 (5), 774 (2013)
16) Webster, N. A. S. et al.: ISIJ Int. 57 (1), 41 (2017)
17) Webster, N. A. S. et al.: ISIJ Int. 59 (6), 1007 (2019)
18) Webster, N. A. S. et al.: ISIJ Int. 59 (2), 263 (2019)
19) Sakamoto, N. et al.: Tetsu-to-Hagané. 70 (6), 504 (1984)
20) Cai, B. et al.: ISIJ Int. 58 (4), 642 (2018)
21) Murakami, T. et al.: ISIJ Int. 60 (12), 2678 (2020)
22) Nicol, S. et al.: ISIJ Int. 58 (12), 2157 (2018)
23) Kimura, M. et al.: Journal of Physics: Conference Series. 430 (1), 012074 (2013)
24) Murao, R. et al.: Tetsu-to-Hagané. 107 (6), 517 (2021)
25) Kimura, M. et al.: Journal of Physics: Conference Series. 712 (1), 012077 (2016)
26) Ravel, B. et al.: J. Synchrotron Rad. 12 (4), 537 (2005)
27) Schuermann, E. et al.: Steel Research. 64, 331 (1993)

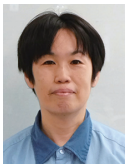

Reiko MURAO
Dr. Eng., Chief Manager, Head of Dept.
Materials Characterization Research Lab.
Advanced Technology Research Laboratories
20-1 Shintomi, Futtsu City, Chiba Pref. 293-8511

Masao KIMURA
Dr. Eng., Professor
Institute of Materials Structure Science,
High Energy Accelerator Research Organization (KEK)
Materials Structure Science Program,
Graduate Institute for Advanced Studies,
SOKENDAI (The Graduate University for Advanced Studies)